SSRG International Journal of Electrical and Electronics Engineering
ISSN: 2348-8379/ https://doi.org/10.14445/23488379/IJEEE-V11I9P119

Volume 11 Issue 9, 216-223, September 2024

Original Article

Analysis of Tapered Circular Waveguide for W Millimeter Wavebands

Reema Budhiraja

Jaypee Institute of Information Technology, Noida, India,

Corresponding Author : reema.budhiraja@jiit.ac.in

Received: 09 July 2024 Revised: 11 August 2024 Accepted: 09 September 2024 Published: 28 September 2024

Abstract *- This manuscript analyzes tapered circular waveguides based on eigen function expansion and the coordinate transformation method. The electromagnetic field configuration is rigorously determined within the tapered circular waveguide by solving a set of coupled ordinary differential equations that account for the variations in the waveguide's geometry and material properties. This detailed approach enables a comprehensive understanding of the distribution and behavior of the electric and magnetic fields in the waveguide, providing valuable insights into the waveguide's performance and characteristics. The concept introduced in this paper specifically focuses on the utilization of tapered waveguide segments with gradually varying taper angles to smoothly transition between waveguides of differing cross-sectional dimensions. This approach aims to optimize the transmission of a specific mode within the waveguide system, enhancing the overall performance and functionality of the waveguide structure. Thus chosen structure is intentionally designed to be smooth, aiming to minimize reflections and reduce mode conversion within the waveguide system.*

Keywords *- Tapered, Electromagnetic, Propagation, Waveguide, Field.*

1. Introduction

Tapered waveguides capable of multimode propagation have gained much interest in the past few years. Tapers are needed in several important applications for long-distance transmissions by employing low loss electric modes in circular waveguides.

Non-uniform tapered waveguide sections are often required in the millimeter wave system to join the two waveguides of distinct radii. The existence of such a taper inevitably leads to undesirable parasitic modes and reflections. The mode matching technique introduced by reference [1] is a powerful technique for analyzing non-uniform waveguides in which a series of uniform waveguide sections replace the real profile. This method consists of matching the field at each joint between uniform segments so that power is conserved.

Dwari in [2] has discussed the analysis of linear tapered waveguides by dividing the taper section into a number of sections having uniform lengths. The results showed that only TE_{10} is propagated along the tapered line. The structure did not support the other modes generated. Jain analyses the non-linear cylindrical taper in [3] for getting the required mode at the end of the output taper for its potential application in high power devices such as gyrotron. Different types of tapers, like exponential, parabolic and raised cosine, were designed using spatial coordinate transformation by Tichit [4]. Kartikeyan studies the optimization algorithm in [5] for the design of a raised cosine taper for 42 GHz, 200KW continuous wave gyrotron operating in the TE_{03} cavity mode. This algorithm is considered fast and accurate for taper analysis. Linear, circular waveguide taper is considered in [6] to measure oversized components transmission attenuation. A large amount of power was found to be converted into spurious modes at resonance frequencies.

In a study examining circular waveguide tapers, researchers investigated the application of Dolph Chebychev tapers as documented in reference [7]. In reference [8], the researchers developed computer codes tailored for the analysis of tapers. These codes were designed to minimize memory usage, expedite convergence for backward modes and simplify the determination of outcomes for forward modes.

A tapered rectangular waveguide is analyzed in [9] for its reflection and transmission characteristics in V to W millimeter wavebands. Large conductor loss was observed due to reflections. Singh analyzes the dispersion characteristics of the tapered structure in [10] for its potential application in gyrotron devices. It is observed that tapering the RF configuration flattens the dispersion curve, and the tapering angle modifies the bandwidth of the configuration but at the price of the device gain.

Lately, there has been a surge in the publication of literature concerning tapered structures. Within these studies, a prominent concern that has been identified is the mode conversion loss that has been associated with tapers, prompting in depth investigation and analysis within the research community. The gradual alteration of waveguide dimensions leads to the generation of spurious modes, which can significantly impact overall system performance.

To address this, waveguide tapers are meticulously engineered with the specific goal of minimizing mode conversion loss, ensuring the effective management of spurious modes and preserving optimal functionality. A well-designed waveguide taper is engineered to effectively transmit all incident power with minimal reflection, ensuring seamless power transfer across various waveguide profiles. The difference in power output arises from a change in the incident mode, which occurs due to the conversion of modes caused by the presence of spurious modes. It is imperative to address and rectify the presence of these unwanted spurious modes.

In the scope of current work, an in-depth analysis has been conducted for weakly tapered non-uniform circular cylindrical waveguides. This involved the utilization of eigen function expansion and coordinate transformation methods to gain a comprehensive understanding of waveguide behavior and characteristics.

The complete set of orthogonal functions has been introduced which are most appropriate to the designed problem. In the present design, the taper is assumed to be sufficiently gradual so that power in all TE_{0n} terms with n greater than one will be significantly smaller than the power in the TE_{01} mode.

In light of the relatively small power coupled from forward waves to backward waves, consideration has been focused solely on forward travelling waves. The design taper is analyzed in terms of propagation characteristics for TE mode to predict its performance.

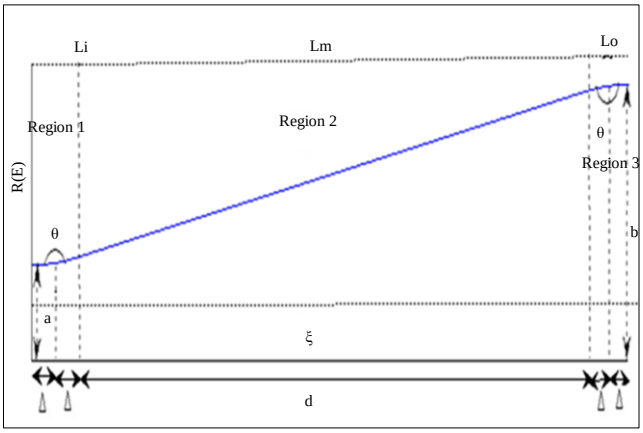

Fig. 1 Geometry of weakly tapered non-uniform circular cylindrical waveguide

2. Tapered Waveguide Design

The design of the circular waveguide involves the intricate configuration of a non-linear waveguide taper section. This design process is executed using MATLAB, a high-level programming and numerical computing environment. In this case, the actual taper profile is replaced by a series of uniform waveguide sections, as clearly depicted in Figure 1.

The incident wave is typically assumed to be TE_{01} mode, which is recognized as the dominant mode of cylindrical waveguides. The non-uniform cylindrical waveguide is structured into three distinct regions to effectively address the boundary value problem of a tapered waveguide transition using the coordinate transformation method. Each region possesses unique widths and heights.

The non-uniform circular cylindrical waveguide's axis is positioned along the $\boldsymbol{\xi}$ coordinate as a part of a transformation of coordinates from $\boldsymbol{F(r,\theta,z)\ to\ \tilde{F}(\zeta,\theta,\xi)}$. The mathematical expressions for three regions are given by,

Region 1: $a + \left(\frac{b-a}{4d\Delta}\right)\xi^2\ for\ \ 0 \le \xi \le 2\Delta$

Region 2: $a - \left(\frac{b-a}{d}\right)\Delta + \left(\frac{b-a}{d}\right)\xi\ for\ \ 2\Delta \le \xi \le \mathrm{d}$

Region3: $b - \left(\frac{b-a}{4d\Delta}\right)(\xi - d - 2\Delta)^2\ for\ \ d \le \xi \le \mathrm{d} + 2\Delta$

The transitions between the three regions are deliberately engineered to feature smooth profiles, with the specific objective of preventing the occurrence of mode conversion that may arise at sharp edges. Additionally, gradual transitions between two waveguides result in minimal reflections and backward propagating waves can be ignored.

3. Analysis

The coordinate transformation has been carefully executed to straighten the tube so that the function R(z) remains constant. This function, R(z), is defined by the resonator profile, and its constancy is crucial for the overall performance. Therefore following transformation have been performed.

$$F(r,\theta,z) = F(\zeta,\theta,\xi)$$

$$\xi = z, \zeta = \frac{ar}{R(z)}\ or\ r = \frac{R(\xi)\zeta}{a}$$

$$\frac{\partial}{\partial z} = \frac{\partial}{\partial \xi} - \frac{R'(\xi)}{R(\xi)}\zeta\frac{\partial}{\partial \zeta}$$

$$\frac{\partial}{\partial \rho} = \frac{a}{R(\xi)}\frac{\partial}{\partial \zeta}$$

$$\frac{\partial^2}{\partial z^2} = \frac{\partial^2}{\partial \xi^2} - \frac{\partial}{\partial \xi}\left(\frac{R'(\xi)}{R(\xi)}\zeta\frac{\partial}{\partial \zeta}\right) - \frac{R'(\xi)}{R(\xi)}\zeta\frac{\partial^2}{\partial \xi \partial z} + \left(\frac{R'(\xi)}{R(\xi)}\right)^2 \zeta\frac{\partial}{\partial \zeta}\left(\zeta\frac{\partial}{\partial \zeta}\right)$$

When modelling the waveguide walls as perfectly conducting, it is imperative to recognize that the non-zero field component depend on specific parameter ξ in accordance with the propagation factor $e^{-j\beta\xi}$ with β propagation phase constant corresponding to single frequency wave propagation in the positive ξ direction. Thus the field component may be formulated as $B(\zeta,\theta,\xi) = b(\zeta,\theta)e^{-j\beta\xi}$. Further, Maxwell's equations can be reformulated in the phasor form as,

$$\left.\begin{array}{c} \nabla \times \tilde{E} = -j\omega\tilde{B} \\ \nabla \times \tilde{B} = -\frac{j\omega\tilde{E}}{c^2} \\ \nabla.\tilde{B} = 0 \\ \nabla.\tilde{E} = \frac{\rho}{\epsilon_0} = 0 \end{array}\right\} \quad (1)$$

The fields in (1) can be decomposed into transverse and axial parts

$$\left.\begin{array}{l} \tilde{E} = \tilde{E}_t + \hat{z}E_z \\ \tilde{B} = \tilde{B}_t + \hat{z}B_z \end{array}\right\} \quad (2)$$

After decomposing, the reduced Maxwell equations for TE modes are,

$$\left(\frac{\partial^2}{\partial z^2} + k_0^2\right)\tilde{B}_t = -\frac{j\omega}{c^2}\hat{z} \times \nabla_t \tilde{E}_z \quad (3)$$

$$\tilde{E}_t = \frac{c^2}{j\omega}\frac{\partial}{\partial z}\left(\hat{z} \times \tilde{B}_t\right) \quad (4)$$

$$\nabla_t^2 \tilde{E}_z + \frac{\partial^2 \tilde{E}_z}{\partial z^2} + k_0^2\tilde{E}_z = 0 \quad (5)$$

Further above expressions are transformed into other coordinates and expanded in terms of axial profile functions given by,

$$\tilde{E}_t(\zeta,\theta,\xi) = \sum_{m,n} A_{mn}^{(h)}(\xi)\underline{e}_{mn}^{(h)}(\zeta,\theta) \quad (6)$$

$$\tilde{B}_t(\zeta,\theta,\xi) = \sum_{m,n} B_{mn}^{(h)}(\xi)\underline{b}_{mn}^{(h)}(\zeta,\theta) \quad (7)$$

$$\tilde{B}_z(\zeta,\theta,\xi) = \sum_{m,n} D_{mn}(\xi)e_{mn}(\zeta,\theta) \quad (8)$$

Here $A_{mn}^{(h)}(\xi)$, $B_{mn}^{(h)}(\xi)$, and $D_{mn}(\xi)$ comprise the axial profile functions. These axial profile functions form an important framework for the present analysis. Further the transverse vector functions $\underline{b}_{mn}^{(h)}$ and $\underline{e}_{mn}^{(h)}$ can be obtained from the scalar mode function b_{mn} as,

$$\boldsymbol{\underline{b}_{mn}^{(h)} = -\tilde{\nabla}_t b_{mn}}$$

$$\boldsymbol{\underline{e}_{mn}^{(h)} = \hat{z} \times \tilde{\nabla}_t b_{mn}}$$

Where,

$\nabla_t = \frac{a}{R(\xi)}\tilde{\nabla}_t$ and ∇_t is the transverse gradient operator.

For a cylindrical waveguide of inner radius a, the scalar function $b_{mn}(\zeta,\theta)$ is given by,

$$b_{mn}(\zeta,\theta) = N_{mn}J_m(k_{mn}\zeta)e^{jm\theta}$$

Where, N_{mn} is normalization constant given by,

$$N_{mn}^{-1} = \sqrt{\pi(\tau_{mn}'^2 - m^2)}J_m(\tau_{mn})$$

And J_m is the m[th] order Bessel function of the first kind. The scalar mode function b_{mn} satisfies the boundary condition.

$$\frac{\partial b_{mn}(a,\theta)}{\partial \zeta} = 0$$

In the above expression, the n[th] zero of the mth order Bessel function of the first kind. $\boldsymbol{J_m'}$ is given by $\boldsymbol{\tau_{mn} \triangleq k_{mn}a}$. The prime notation indicates the derivative with respect to the function's argument and $\boldsymbol{\tau_{mn}}$ is the cut-off wave number of mn[th] TE mode.

The wave equation for TE mode in cylindrical coordinates is given by,

$$\nabla_t^2 B_z + \frac{\partial^2}{\partial z^2}B_z + k_0^2 B_z = 0 \quad (9)$$

Through the transformation of coordinates, a set of three coupled ordinary differential equations are obtained from the above equation, which are expressed in terms of axial profile functions $\boldsymbol{\bar{A}_{mn}^h(\bar{\xi})}$ $\boldsymbol{\bar{B}_{mn}^h(\bar{\xi})}$ and $\boldsymbol{\bar{D}_{mn}(\bar{\xi})}$.

$$= \frac{d^2}{d\bar{\xi}^2}\bar{A}_{mk}^h(\bar{\xi}) + \bar{A}_{mn}^h(\bar{\xi}) - 2\frac{\bar{R}'(\xi)}{\bar{R}(\bar{\xi})}\sum_k \frac{d}{d\bar{\xi}}\bar{A}_{mk}^h(\bar{\xi})\Omega_{mnk}^{(h)}$$

$$= \sum_k \bar{A}_{mk}^h(\bar{\xi})\Omega_{mnk}^{(h)}\left(\frac{\bar{R}''(\bar{\xi})}{\bar{R}(\bar{\xi})} - 2\left(\frac{\bar{R}'(\bar{\xi})}{\bar{R}(\bar{\xi})}\right)^2\right) + \left(\frac{\bar{R}'(\bar{\xi})}{\bar{R}(\bar{\xi})}\right)^2 U_{mnk}^h \sum_k \bar{A}_{mk}^h(\bar{\xi}) + \frac{1}{\bar{R}(\bar{\xi})} j\bar{D}_{mn}(\bar{\xi}) \quad (10)$$

$$\bar{B}_{mn}^h(\bar{\xi}) = \frac{1}{j}\left[\frac{d}{d\bar{\xi}}\bar{A}_{mn}^h(\bar{\xi}) - \frac{\bar{R}'(\bar{\xi})}{\bar{R}(\bar{\xi})}\sum_k \bar{A}_{mk}^h(\bar{\xi})\Omega_{mnk}^{(h)}\right] \quad (11)$$

$$= \frac{d^2}{d\xi^2}\bar{D}_{mn}(\bar{\xi}) + \left(1 - \frac{\hat{k}_{mn}^2}{\bar{R}^2(\bar{\xi})}\right)\bar{D}_{mn}(\bar{\xi}) - 2\frac{\bar{R}'(\bar{\xi})}{\bar{R}(\bar{\xi})}\sum_k \frac{d}{d\bar{\xi}}\bar{D}_{mk}(\bar{\xi})\Gamma_{mnk}^{(h)}$$

$$= \left[\frac{\bar{R}''(\bar{\xi})}{\bar{R}(\bar{\xi})} + 2\left(\frac{\bar{R}'(\bar{\xi})}{\bar{R}(\bar{\xi})}\right)^2\right]\sum_k \bar{D}_{mk}(\bar{\xi})\Gamma_{mnk}^{(h)} - \left(\frac{\bar{R}'(\bar{\xi})}{\bar{R}(\bar{\xi})}\right)^2 \sum_k \bar{D}_{mk}(\bar{\xi})\Lambda_{mnk}^{(h)} \quad (12)$$

Where,

$$\bar{A}_{mn}^{(h)}(\bar{\xi}) = \frac{\omega}{c^2}\frac{A_{mn}^{(h)}((\xi))}{\bar{D}_{01}(0)},$$

$$\bar{D}_{mn}(\bar{\xi}) = \frac{D_{mn}(\xi)}{\bar{D}_{01}(0)},$$

$$\bar{B}_{mn}^{(h)}(\bar{\xi}) = k_0\frac{B_{mn}^{(h)}(\xi)}{\bar{D}_{01}(0)}$$

The mode coupling coefficients in the above equations are given by,

$$\Gamma_{mnk}^{(h)} = \begin{cases} -2\pi\tilde{N}_{mn}\tilde{N}_{mk}\tilde{x}_{mk}^3\tilde{I}_{mnk}^{(2)} \ for\ n \neq k \\ 2\pi\left|\tilde{N}_{mn}\right|^2\left[\tilde{x}_{mn}^2\left\{\frac{m}{2}\left(1 - \frac{m^2}{\tilde{x}_{mn}^2}\right)J_m^2(\tilde{x}_{mn})\right\} - x_{mn}^3\tilde{I}_{mnn}^{(2)}\right] for\ n = k \end{cases}$$

$$\Lambda_{mnk}^{(h)} = \begin{cases} 2\pi\tilde{N}_{mn}\tilde{N}_{mk}(\tilde{x}_{mk}^3\tilde{I}_{mnk}^{(2)} - \tilde{x}_{mk}^4\tilde{I}_{mkn}^{(3)}) \\ for\ n \neq k \\ 2\pi\left|\tilde{N}_{mn}\right|^2\left(\left(\frac{-m+m^2}{2}\right)\tilde{x}_{mn}^2 + \left(1 - \frac{m^2}{\tilde{x}_{mn}^2}\right)J_m^2(\tilde{x}_{mn}) + \tilde{x}_{mn}^3\tilde{I}_{mnn}^2 - \tilde{x}_{mn}^4\tilde{I}_{mnn}^{(3)}\right) \\ for\ n = k \end{cases}$$

$$\Omega_{mnk}^{(h)} = 2\pi\tilde{N}_{mn}\tilde{N}_{mk}\left[\left(m^2 - \frac{1}{2}m\right)J_m(\tilde{x}_{mn})J_m(\tilde{x}_{mk})\frac{1}{2} + \frac{\tilde{x}_{mk}\tilde{x}_{mn}}{(x_{mk}^2 - x_{mn}^2)}\begin{Bmatrix}\tilde{x}_{mk}J_{m+1}(\tilde{x}_{mn})J_{m+2}(\tilde{x}_{mk}) \\ -\tilde{x}_{mn}J_{m+1}(\tilde{x}_{mk})J_{m+2}(\tilde{x}_{mn})\end{Bmatrix} + \tilde{x}_{mk}^2\tilde{x}_{mn}\tilde{I}_{mkn}^{(2)}\right] for\ n \neq k$$

$$2\pi\left|\tilde{N}_{mn}\right|^2\left\{J_m^2(\tilde{x}_{mn})\left[2m^2 - \tilde{x}_{mn}^2 + \frac{m^3}{2}\right] + \frac{\tilde{x}_{mn}^2}{4}[J_{m-1}^2(\tilde{x}_{mn})] + \tilde{x}_{mn}^3\tilde{I}_{mnn}^{(2)} + J_{m+1}^2(\tilde{x}_{mn})\right\} for\ n = k$$

$$\Delta_{mnk}^{(h)} = 2\pi\tilde{N}_{mn}\tilde{N}_{mk}\left\{\begin{array}{c}\left(\frac{m^2}{4} - \frac{1}{2}\right)J_m(\tilde{x}_{mn})J_m(\tilde{x}_{mk}) + \frac{(2+m^2)}{4}\frac{\tilde{x}_{mk}\tilde{x}_{mn}}{\tilde{x}_{mk}^2 - \tilde{x}_{mn}^2}\begin{bmatrix}\tilde{x}_{mk}J_{m+1}(\tilde{x}_{mn})J_{m+2}(\tilde{x}_{mk}) \\ -\tilde{x}_{mn}J_{m+1}(\tilde{x}_{mk})J_{m+2}(\tilde{x}_{mn})\end{bmatrix} \\ -(1-m)\tilde{x}_{mk}^2\tilde{I}_{mkn}^{(2)} - 2m^3\tilde{I}_{mnk}^{(-1)} + 2m^2\tilde{x}_{mn}\tilde{I}_{mkn}^{(0)} + m\tilde{x}_{mk}^3\tilde{I}_{mnk}^{(2)}\end{array}\right\} for\ n \neq k$$

$$2\pi\left|\tilde{N}_{mn}\right|^2 \frac{\tilde{\boldsymbol{x}}_{\boldsymbol{mn}}^{\boldsymbol{2}}(\boldsymbol{2}+\boldsymbol{m}^{\boldsymbol{2}})}{\boldsymbol{8}}\left[\boldsymbol{m}^{\boldsymbol{2}}\boldsymbol{J}_{\boldsymbol{m}}^{\boldsymbol{2}}(\tilde{\boldsymbol{x}}_{\boldsymbol{mn}}) + \frac{\tilde{\boldsymbol{x}}_{\boldsymbol{mn}}^{\boldsymbol{2}}}{\boldsymbol{2}}\boldsymbol{J}_{\boldsymbol{m}}^{\boldsymbol{2}}(\tilde{\boldsymbol{x}}_{\boldsymbol{mn}}) + \boldsymbol{J}_{\boldsymbol{m-1}}^{\boldsymbol{2}}(\tilde{\boldsymbol{x}}_{\boldsymbol{mn}}) + \boldsymbol{J}_{\boldsymbol{m+1}}^{\boldsymbol{2}}(\tilde{\boldsymbol{x}}_{\boldsymbol{mn}})\right] + (\boldsymbol{m}-\boldsymbol{2m}^{\boldsymbol{2}})\frac{\tilde{\boldsymbol{x}}_{\boldsymbol{mn}}^{\boldsymbol{2}}}{\boldsymbol{2}}\left[\boldsymbol{1} - \frac{\boldsymbol{m}^{\boldsymbol{2}}}{\tilde{\boldsymbol{x}}_{\boldsymbol{mn}}^{\boldsymbol{2}}}\right]\boldsymbol{J}_{\boldsymbol{m}}^{\boldsymbol{2}}(\tilde{\boldsymbol{x}}_{\boldsymbol{mn}}) + (\boldsymbol{2m}-\boldsymbol{1})\tilde{\boldsymbol{x}}_{\boldsymbol{mn}}^{\boldsymbol{3}}\tilde{\boldsymbol{I}}_{\boldsymbol{mnn}}^{(\boldsymbol{2})} - \boldsymbol{2m}^{\boldsymbol{3}}\tilde{\boldsymbol{I}}_{\boldsymbol{mnn}}^{(\boldsymbol{-1})} + \boldsymbol{2m}^{\boldsymbol{2}}\tilde{\boldsymbol{x}}_{\boldsymbol{mn}}\tilde{\boldsymbol{I}}_{\boldsymbol{mnn}}^{(\boldsymbol{0})} - \tilde{\boldsymbol{x}}_{\boldsymbol{mn}}^{\boldsymbol{4}}\tilde{\boldsymbol{I}}_{\boldsymbol{mn}}^{(\boldsymbol{3})} - \boldsymbol{J}_{\boldsymbol{m}}^{\boldsymbol{2}}(\tilde{\boldsymbol{x}}_{\boldsymbol{mn}}) \ \boldsymbol{for\ n = k}$$

Where,

$$\boldsymbol{1.}\ \tilde{\boldsymbol{I}}_{\boldsymbol{mkn}}^{(\boldsymbol{2})} = \int_0^1 \boldsymbol{y}^{\boldsymbol{2}}\boldsymbol{J}_{\boldsymbol{m}}(\tilde{\boldsymbol{x}}_{\boldsymbol{mk}}\boldsymbol{y})\boldsymbol{J}_{\boldsymbol{m+1}}(\tilde{\boldsymbol{x}}_{\boldsymbol{mn}}\boldsymbol{y})\boldsymbol{dy}$$

$$2.\ \tilde{I}_{mnn}^{(2)} = \int_0^1 y^2 J_m(\tilde{x}_{mn}y)J_{m+1}(\tilde{x}_{mn}y)dy$$

$$3.\ \tilde{I}_{mnk}^{(-1)} = \int_0^1 \frac{1}{y}J_m(\tilde{x}_{mk}y)J_m(\tilde{x}_{mn}y)dy$$

4. $\tilde{I}_{mkn}^{(0)} = \int_0^1 J_m(\tilde{x}_{mk}y)J_{m+1}(\tilde{x}_{mn}y)dy$

5. $\tilde{I}_{mnk}^{(2)} = \int_0^1 y^2 J_{m+1}(\tilde{x}_{mk}y)J_m(\tilde{x}_{mn}y)dy$

6. $\tilde{I}_{mnn}^{(-1)} = \int_0^1 \frac{1}{y} J_m^2(\tilde{x}_{mn}y)dy$

7. $\tilde{\boldsymbol{I}}_{\boldsymbol{mn}}^{(\mathbf{3})} = \int_0^1 \boldsymbol{y^3 J_{m+1}^2(\tilde{x}_{mn}y)dy}$

8. $\tilde{\boldsymbol{I}}_{\boldsymbol{mkn}}^{(\mathbf{3})} = \tilde{\boldsymbol{I}}_{\boldsymbol{mnk}}^{(\mathbf{3})} = \int_0^1 \boldsymbol{y^3 J_m(\tilde{x}_{mk}y)J_m(\tilde{x}_{mn}y)dy}$

9. $\tilde{I}_{mnn}^{(3)} = \int_0^1 y^3 J_m^2(\tilde{x}_{mn}y)\, dy$

10. $\tilde{I}_{mnn}^{(0)} = \int_0^1 J_m(\tilde{x}_{mn}y)J_{m+1}(\tilde{x}_{mn}y)dy$

4. Numerical Solution of Differential Equations

The complex electromagnetic field configuration inside an irregular waveguide is accurately determined by employing numerical methods to solve the coupled ordinary differential equations governing the axial profile functions specific to the TE mode. This process helps in understanding how the electromagnetic waves propagate and behave within the irregular waveguide structure. The field strength is determined based on the specific signaling condition that denotes the initial strength of the mode that excites the waveguide. Further, to solve the system of coupled ordinary differential equations, the first step involves expressing the equations in matrix form. After this, the coefficient matrix is diagonalized to separate and simplify the equations.

Defining

$$\underline{\boldsymbol{\Gamma}}_{\boldsymbol{m}}^{(\boldsymbol{h})} = \left[\boldsymbol{\Gamma}_{\boldsymbol{mnk}}^{(\boldsymbol{h})}\right]_{\mathbf{1}\le \boldsymbol{n,k}\le \boldsymbol{n}} \quad (\boldsymbol{N \times N\ matrix})$$

$$\underline{\bar{\boldsymbol{D}}}_{\boldsymbol{m}}(\bar{\xi}) = \left[\bar{\boldsymbol{D}}_{\boldsymbol{m1}}(\bar{\xi}), \bar{\boldsymbol{D}}_{\boldsymbol{m2}}(\bar{\xi}), \bar{\boldsymbol{D}}_{\boldsymbol{m3}}(\bar{\xi}) \dots\dots\dots \bar{\boldsymbol{D}}_{\boldsymbol{mN}}(\bar{\xi})\right]^{\boldsymbol{T}}$$

$$\underline{\boldsymbol{S}}_{\boldsymbol{m}}^{(\boldsymbol{h})-\mathbf{1}}\underline{\boldsymbol{\Gamma}}_{\boldsymbol{m}}^{(\boldsymbol{h})}\underline{\boldsymbol{S}}_{\boldsymbol{m}}^{(\boldsymbol{h})} = \boldsymbol{Diag}\left[\boldsymbol{\lambda}_{\boldsymbol{m1}}^{(\boldsymbol{h})}, \boldsymbol{\lambda}_{\boldsymbol{m2}}^{(\boldsymbol{h})} \dots\dots\dots\dots\dots \boldsymbol{\lambda}_{\boldsymbol{mN}}^{(\boldsymbol{h})}\right]$$

Where, $Re\lambda_{m1}^{(h)} \ge Re\lambda_{m2}^{(h)} \ge Re\lambda_{mn}^{(h)}$.

In the expression mentioned above, the symbols $\boldsymbol{\lambda}_{\boldsymbol{mN}}^{(\boldsymbol{h})}$ and $\underline{S}_m^{(h)}$represent the specific eigenvalues and corresponding eigenvectors of the coefficient matrix $\underline{\Gamma}_m^{(h)}$. Additionally, the notation "Diag" signifies the diagonalization process of a matrix, while "T" denotes the transpose of the matrix. Writing axial profile function $\underline{\bar{D}}_m(\bar{\xi})$ in terms of eigenvectors the expression obtained is,

$$\underline{\bar{D}}_m(\bar{\xi}) = \underline{S}_m^{(h)}\underline{U}_m(\bar{\xi})$$

$$\underline{\boldsymbol{U}}_{\boldsymbol{m}}(\bar{\boldsymbol{\xi}}) = \underline{\boldsymbol{S}}_{\boldsymbol{m}}^{(\boldsymbol{h})-\mathbf{1}}\underline{\bar{\boldsymbol{D}}}_{\boldsymbol{m}}(\bar{\boldsymbol{\xi}})$$

Where, $\underline{S}_m^{(h)-1}$ is the inverse of the eigenvectors.

Substituting the value of the axial profile function following expression is obtained.

$$\begin{aligned}\underline{S}_m^{(h)}\underline{U}_m''(\bar{\xi}) - 2\frac{\bar{R}'(\bar{\xi})}{\bar{R}(\bar{\xi})}\underline{\Gamma}_m^{(h)}\underline{S}_m^{(h)}\underline{U}_m'(\bar{\xi}) = \\ -\underline{S}_m^{(h)}\underline{U}_m(\bar{\xi}) + \frac{1}{\bar{R}^2(\bar{\xi})}diag(\hat{k}_{mn}^2)\underline{S}_m^{(h)}\underline{U}_m'(\bar{\xi}) \\ + \left[\frac{\bar{R}''(\bar{\xi})}{\bar{R}(\bar{\xi})} - 2\left(\frac{\bar{R}'(\bar{\xi})}{\bar{R}(\bar{\xi})}\right)^2\right]\underline{\boldsymbol{\Gamma}}_{\boldsymbol{m}}^{(\boldsymbol{h})}\underline{\boldsymbol{S}}_{\boldsymbol{m}}^{(\boldsymbol{h})}\underline{\boldsymbol{U}}_{\boldsymbol{m}}(\bar{\boldsymbol{\xi}}) \\ -\left(\frac{\bar{R}'(\bar{\xi})}{\bar{R}(\bar{\xi})}\right)^2\underline{\Lambda}_m^{(h)}\underline{S}_m^{(h)}\underline{U}_m(\bar{\xi}) \end{aligned} \quad (13)$$

Premultiplying the expression (13) by$\underline{S}_m^{(h)-1}$ yields,

$$\begin{aligned}&\underline{U}_m''(\bar{\xi}) - 2\frac{\bar{R}'(\bar{\xi})}{\bar{R}(\bar{\xi})}diag\lambda_{mn}^{(h)}\underline{U}_m'(\bar{\xi}) = \\ &\begin{bmatrix} -\underline{\boldsymbol{I}}_{\boldsymbol{n}} + \frac{\mathbf{1}}{\bar{\boldsymbol{R}}^{\boldsymbol{2}}(\bar{\boldsymbol{\xi}})}\underline{\boldsymbol{S}}_{\boldsymbol{m}}^{(\boldsymbol{h})-\mathbf{1}}\boldsymbol{diag}(\hat{\boldsymbol{k}}_{\boldsymbol{mn}}^{\boldsymbol{2}})\underline{\boldsymbol{S}}_{\boldsymbol{m}}^{(\boldsymbol{h})} \\ +\left(\frac{\bar{\boldsymbol{R}}''(\bar{\boldsymbol{\xi}})}{\bar{\boldsymbol{R}}(\bar{\boldsymbol{\xi}})} - \mathbf{2}\left(\frac{\bar{\boldsymbol{R}}'(\bar{\boldsymbol{\xi}})}{\bar{\boldsymbol{R}}(\bar{\boldsymbol{\xi}})}\right)^{\mathbf{2}}\right)\boldsymbol{diag}(\boldsymbol{\lambda}_{\boldsymbol{mn}}^{(\boldsymbol{h})}) \\ -\left(\frac{\bar{\boldsymbol{R}}'(\bar{\boldsymbol{\xi}})}{\bar{\boldsymbol{R}}(\bar{\boldsymbol{\xi}})}\right)^{\mathbf{2}}\underline{\boldsymbol{S}}_{\boldsymbol{m}}^{(\boldsymbol{h})-\mathbf{1}}\underline{\boldsymbol{\Lambda}}_{\boldsymbol{m}}^{(\boldsymbol{h})}\underline{\boldsymbol{S}}_{\boldsymbol{m}}^{(\boldsymbol{h})} \end{bmatrix}\underline{\boldsymbol{U}}_{\boldsymbol{m}}(\bar{\boldsymbol{\xi}}) \end{aligned} \quad (14)$$

Here $-\underline{I}_n$ is the identity matrix. Solving further coupled vector integral equation is obtained in terms of axial profile function $\underline{D}_m(\bar{\xi})$.

$$\begin{aligned}&\underline{U}_m(\bar{\xi}) = \underline{U}_m(0) + U_m'(0)diag\int_0^{\bar{\xi}}\left(\bar{R}(y)\right)^{2\lambda_{mn}^{(h)}}dy + \\ &\int_0^{\bar{\xi}}\underline{K}_m^{(h)}(\bar{\xi},y)\underline{U}_m(y)dy \end{aligned} \quad (15)$$

Here,

$$\underline{\boldsymbol{K}}_{\boldsymbol{m}}^{(\boldsymbol{h})}(\bar{\boldsymbol{\xi}},\boldsymbol{y}) \triangleq \underline{\boldsymbol{diag}}\left(\boldsymbol{K}_{\boldsymbol{mn}}^{(\boldsymbol{h})}(\bar{\boldsymbol{\xi}},\boldsymbol{y})\right)\underline{\boldsymbol{M}}_{\boldsymbol{m}}^{(\boldsymbol{h})}(\boldsymbol{y})$$

$$\boldsymbol{K}_{\boldsymbol{mn}}^{(\boldsymbol{h})}(\bar{\boldsymbol{\xi}},\boldsymbol{y}) \triangleq \int_{\boldsymbol{y}}^{\xi}\left(\frac{\bar{\boldsymbol{R}}(\boldsymbol{x})}{\bar{\boldsymbol{R}}(\boldsymbol{y})}\right)^{\mathbf{2}\boldsymbol{\lambda}_{\boldsymbol{mn}}^{(\boldsymbol{h})}}\boldsymbol{dx}$$

$$\underline{\boldsymbol{M}}_{\boldsymbol{m}}^{(\boldsymbol{h})}(\boldsymbol{y}) = \begin{bmatrix} -\underline{\boldsymbol{I}}_{\boldsymbol{n}} + \frac{\mathbf{1}}{\bar{\boldsymbol{R}}^{\boldsymbol{2}}(\bar{\boldsymbol{\xi}})}\underline{\boldsymbol{S}}_{\boldsymbol{m}}^{(\boldsymbol{h})-\mathbf{1}}\boldsymbol{diag}(\hat{\boldsymbol{k}}_{\boldsymbol{mn}}^{\boldsymbol{2}})\underline{\boldsymbol{S}}_{\boldsymbol{m}}^{(\boldsymbol{h})} \\ +\left(\frac{\bar{\boldsymbol{R}}''(\bar{\boldsymbol{\xi}})}{\bar{\boldsymbol{R}}(\bar{\boldsymbol{\xi}})} - \mathbf{2}\left(\frac{\bar{\boldsymbol{R}}'(\bar{\boldsymbol{\xi}})}{\bar{\boldsymbol{R}}(\bar{\boldsymbol{\xi}})}\right)^{\mathbf{2}}\right)\boldsymbol{diag}(\boldsymbol{\lambda}_{\boldsymbol{mn}}^{(\boldsymbol{h})}) \\ -\left(\frac{\bar{\boldsymbol{R}}'(\bar{\boldsymbol{\xi}})}{\bar{\boldsymbol{R}}(\bar{\boldsymbol{\xi}})}\right)^{\mathbf{2}}\underline{\boldsymbol{S}}_{\boldsymbol{m}}^{(\boldsymbol{h})-\mathbf{1}}\underline{\boldsymbol{\Lambda}}_{\boldsymbol{m}}^{(\boldsymbol{h})}\underline{\boldsymbol{S}}_{\boldsymbol{m}}^{(\boldsymbol{h})} \end{bmatrix}\underline{\boldsymbol{U}}_{\boldsymbol{m}}(\boldsymbol{y})$$

Similarly, solving for $\underline{\bar{B}}_m^{(h)}(\bar{\xi})$ the expression obtained is,

$$\underline{\boldsymbol{W}}_{\boldsymbol{m}}^{(\boldsymbol{h})}(\bar{\boldsymbol{\xi}}) = \underline{\boldsymbol{W}}_{\boldsymbol{m}}^{(\boldsymbol{h})}(\mathbf{0}) + \underline{\boldsymbol{W}}_{\boldsymbol{m}}^{(\boldsymbol{h})'}(\mathbf{0})\boldsymbol{diag}\int_{\mathbf{0}}^{\bar{\boldsymbol{\xi}}}\left(\boldsymbol{R}(\boldsymbol{y})\right)^{2\boldsymbol{\lambda}_{\boldsymbol{mn}}^{(\boldsymbol{h})}}\boldsymbol{dy} + \int_0^{\bar{\xi}} diag(L_{mn}^{(h)}(\bar{\xi},y))\underline{V}_m^{(h)}(y)\underline{W}_m^{(h)}(y)dy + \int_0^{\bar{\xi}} diag(L_{mn}^{(h)}(\bar{\xi},y))\underline{P}_m^{(h)}(y)dy \quad (16)$$

Here, $\underline{\bar{\boldsymbol{B}}}_{\boldsymbol{m}}^{(\boldsymbol{h})}(\bar{\boldsymbol{\xi}}) = \underline{\boldsymbol{Q}}_{\boldsymbol{m}}^{(\boldsymbol{h})}\underline{\boldsymbol{W}}_{\boldsymbol{m}}^{(\boldsymbol{h})}(\bar{\boldsymbol{\xi}})$

$$\boldsymbol{L}_{\boldsymbol{mn}}^{(\boldsymbol{h})}(\bar{\boldsymbol{\xi}},\boldsymbol{y}) \triangleq \int_{\boldsymbol{y}}^{\bar{\boldsymbol{\xi}}}\left(\frac{\bar{\boldsymbol{R}}(\boldsymbol{x})}{\bar{\boldsymbol{R}}(\boldsymbol{y})}\right)^{2\boldsymbol{\lambda}_{\boldsymbol{mn}}^{(\boldsymbol{h})}}\boldsymbol{dx}$$

$$\underline{\boldsymbol{V}}_{\boldsymbol{m}}^{(\boldsymbol{h})}(\boldsymbol{y}) = \frac{\boldsymbol{j}}{\bar{\boldsymbol{R}}(\boldsymbol{y})}\underline{\boldsymbol{Q}}_{\boldsymbol{m}}^{(\boldsymbol{h})-\mathbf{1}}\underline{\boldsymbol{S}}_{\boldsymbol{m}}^{\boldsymbol{h}}\underline{\boldsymbol{U}}_{\boldsymbol{m}}(\bar{\boldsymbol{\xi}})$$

and

$$\underline{\boldsymbol{P}}_{\boldsymbol{m}}^{(\boldsymbol{e})}(\boldsymbol{y}) = \left[-\underline{\boldsymbol{I}}_{\boldsymbol{n}} + \left(\frac{\bar{\boldsymbol{R}}''(\bar{\boldsymbol{\xi}})}{\bar{\boldsymbol{R}}(\bar{\boldsymbol{\xi}})} - \mathbf{2}\left(\frac{\bar{\boldsymbol{R}}'(\bar{\boldsymbol{\xi}})}{\bar{\boldsymbol{R}}(\bar{\boldsymbol{\xi}})}\right)^{\mathbf{2}}\right)\boldsymbol{diag}\left(\boldsymbol{\lambda}_{\boldsymbol{mn}}^{(\boldsymbol{h})}\right) - \left(\frac{\bar{\boldsymbol{R}}'(\bar{\boldsymbol{\xi}})}{\bar{\boldsymbol{R}}(\bar{\boldsymbol{\xi}})}\right)^{\mathbf{2}}\underline{\boldsymbol{Q}}_{\boldsymbol{m}}^{(\boldsymbol{h})-\mathbf{1}}\underline{\boldsymbol{\Lambda}}_{\boldsymbol{m}}^{(\boldsymbol{h})}\underline{\boldsymbol{Q}}_{\boldsymbol{m}}^{(\boldsymbol{h})}\right]\underline{\boldsymbol{W}}_{\boldsymbol{m}}^{(\boldsymbol{h})}(\boldsymbol{y})$$

With $\underline{\boldsymbol{Q}}_{\boldsymbol{m}}^{(\boldsymbol{h})}$ being the eigenvectors of the matrix $\underline{\boldsymbol{\Omega}}_{\boldsymbol{m}}^{(\boldsymbol{h})} \triangleq \left[\underline{\boldsymbol{\Omega}}_{\boldsymbol{mnk}}^{(\boldsymbol{h})}\right]_{\mathbf{1}\leq\boldsymbol{n},\boldsymbol{k}\leq\boldsymbol{n}}$.

This paper numerically computes the field profiles only for the axisymmetric TE0 modes, as these modes are found to be ideally suited to be employed in high-power devices.

5. Results

A non-linear cylindrical waveguide has been considered, which is excited in TE mode for use as an output taper for getting the required mode at the end of the output taper. These equations have been carefully solved while considering the specific boundary conditions that are relevant to the waveguide's geometry and material properties.

In order to accurately ascertain the electromagnetic field within a perfectly conducting curved waveguide with non-uniform and arbitrary cross-sectional properties, a systematic and rigorous solution was achieved through the resolution of a set of coupled ordinary differential equations. Here, the defined field problem involves a complex boundary, but it can be more effectively addressed through a coordinate transformation.

This transformation converts the irregular waveguide into a regular waveguide in a new coordinate system. Numerical results are obtained for a weakly tapered waveguide whose operating frequency is 94 GHz. This frequency is specifically chosen due to the fact that high-power devices offer superior performance when operating through clouds, fog, and smoke at this particular frequency.

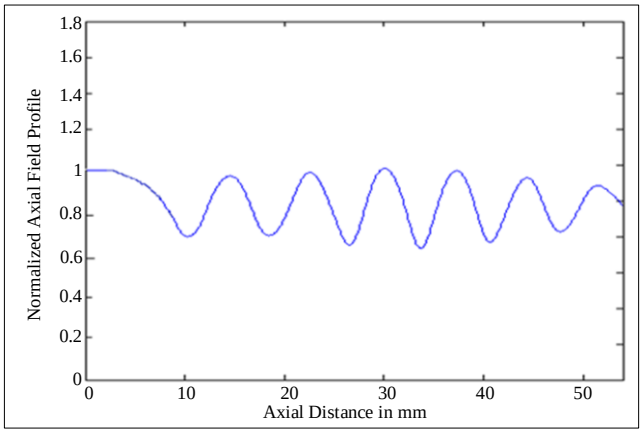

Fig. 2 Magnitude of TE_{01} mode's field profile

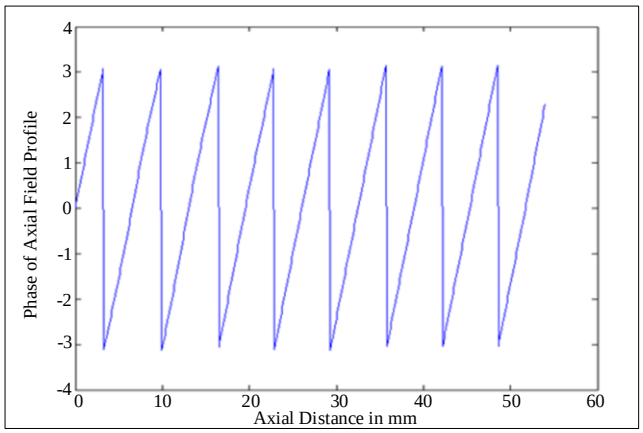

Fig. 3 Phase of TE_{01} mode's field profile

This frequency allows for effective transmission and reception of signals even in adverse weather conditions, making it a practical and reliable choice for various applications. Here are the additional detailed design specifications: The operating mode is TE_{01}, with the waveguide radius having values a = 3.06 mm and b = 5.88 mm.

Additionally, the lengths of the input, middle, and output sections are specified as L_i = 4 mm, L_m = 46 mm, and L_o = 4 mm, respectively. Furthermore, the angles of the input and output taper are given by $\theta_i = 10^0, \theta_{o=}10^0$.

From the obtained numerical results, it is observed that the main incident power is carried by one specific mode, i.e. TE_{01}, as shown in Figure 2. Further Figures 4, 5, 6, and 7 show that the amplitudes of other modes, i.e. TE_{02}, TE_{03}, TE_{04}, TE_{05}, are maintained very small, thus maintaining high mode purity.

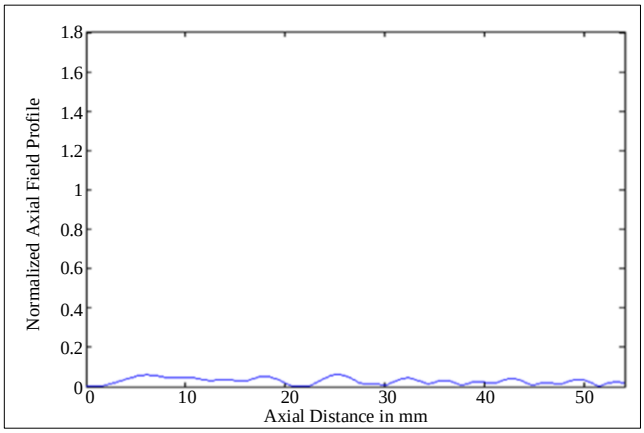

Fig. 4 Magnitude of TE_{02} mode's field profile

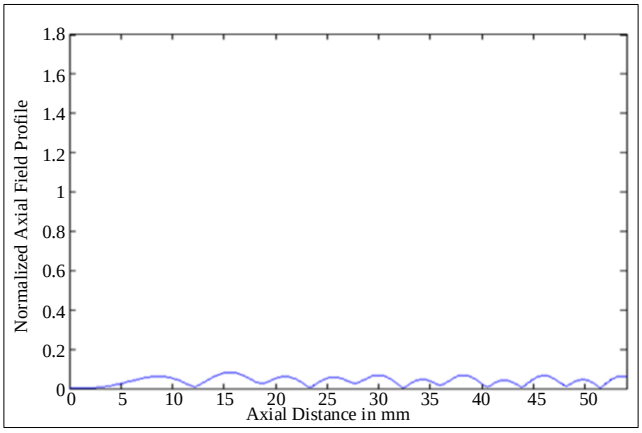

Fig. 5 Magnitude of TE_{03} mode's field profile

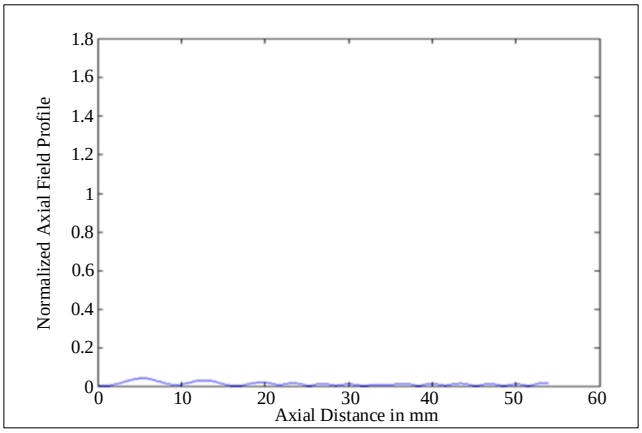

Fig. 6 Magnitude of TE_{04} mode's field profile

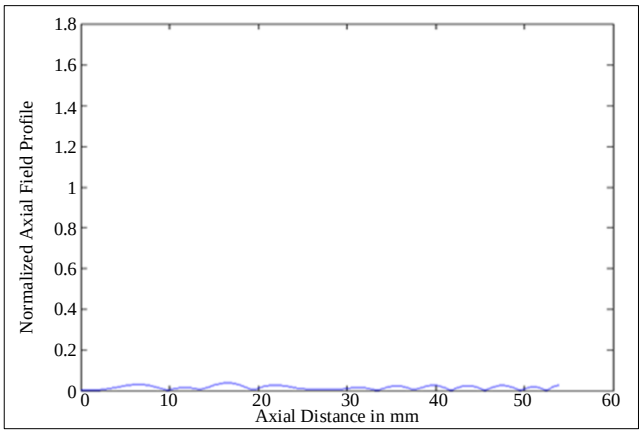

Fig. 7 Magnitude of TE_{05} mode's field profile

The radiation produced in the primary section of the interaction area, which is region 2, as shown in Figure 1, demonstrates oscillations accompanied by a continuous increase in amplitude, as shown in Figure 2, underscoring the dynamic and impactful nature of the electromagnetic phenomena occurring within this domain.

As one progresses towards the output section, the sustained oscillations show only a slight decrease in amplitude, as depicted in Figure 2. Additionally, Figure 3 provides a detailed visual representation of the phase of an electromagnetic field configuration specifically within the TE_{01} mode, allowing for a more comprehensive understanding of the mode characteristics.

6. Conclusion

The electromagnetic boundary value problem has been solved for non-uniform weakly tapered cylindrical waveguides using eigen function expansion and coordinate transformation method. Results have been successfully obtained for the Radio Frequency (RF) field distribution of the TE_{mn} modes, focusing specifically on the transition from a straight section with a non-uniform cross-section to a section with a non-linear up-taper. This comprehensive analysis provides valuable insights into the performance and behavior of the waveguide structure. Upon further analysis, it has been discovered that the newly proposed taper design demonstrates exceptional suitability due to its minimal shape variation at both ends.

This unique feature not only leads to minimal reflections but also enables maximum transmission in the desired mode while simultaneously achieving a substantial reduction in mode conversion when compared to existing taper designs documented in the literature. Hence, the findings from this analysis will be highly beneficial to microwave practitioners, providing valuable insights for the analysis and design of efficient non-linear tapers. These insights will assist practitioners in the selection and adaptation of the final contours for high-power microwave or millimeter-wave devices and systems, ultimately contributing to enhanced overall performance and functionality.

References

[1] D.S. Nagarkoti et al., "Analysis of Non-Linear Cylindrical Waveguide Taper Using Modal Matching Technique," *International Journal of Microwave Applications*, vol. 1, no. 1, pp. 2320-2599, 2012. [Google Scholar] [Publisher Link]

[2] Santanu Dwari, Ajay Chakraborty, and Subrata Sanyal, "Analysis of Linear Tapered Waveguide by Two Approaches," *Progress In Electromagnetics Research*, vol. 4, pp. 219-238, 2006. [CrossRef] [Google Scholar] [Publisher Link]

[3] Smrity Dwivedi, Deepak S. Nagarkoti, and P.K. Jain, "Analysis and Design of Non-Linear Cylindrical Tapers for High Power Devices," *Indian Conference on Microwaves, Antenna, Propagation and Remote Sensing (InCMARS)*, pp. 1-9, 2008. [Google Scholar]

[4] Paul-Henri Tichit, Shah Nawaz Burokur, and Andre de Lustrac, "Waveguide Taper Engineering Using Coordinate Transformation Technology," *Optics Express*, vol. 18, no. 2, pp. 767-772, 2010. [CrossRef] [Google Scholar] [Publisher Link]

[5] Narendra Chauhan et al., "Design and Optimization of Non-Linear Taper Using Particle Swarm Optimization," *International Journal of Infrared and Millimeter Waves*, vol. 29, pp.792-798, 2008. [CrossRef] [Google Scholar] [Publisher Link]

[6] Krupali D. Donda, Ravinder Kumar, and Hiteshkumar B. Pandya, "Design, Devlopment and Testing of Circular Waveguide Taper for Millimeter Wave Transmission Line," *International Journal of Microwave Applications*, vol.4, no. 4, pp. 22-25, 2015. [Google Scholar] [Publisher Link]

[7] H. Flugel, and E. Kuhn, "Computer Aided Analysis and Design of Circular Waveguide Tapers," *IEEE Transactions on Microwave theory and Techniques*, vol. 36, no. 2, pp. 332-336, 1988. [CrossRef] [Google Scholar] [Publisher Link]

[8] W.G. Lawson, "Theoretical Evaluation of Non-Linear Tapers for a High Power Gyrotrons," *IEEE Transactions on Microwave Theory and Techniques*, vol. 38, no. 11, pp. 1617-1622, 1990. [CrossRef] [Google Scholar] [Publisher Link]

[9] Sangsu Lee et al., "Analysis of a Tapered Rectangular Waveguide for V to W Millimeter Wavebands," *Journal of Electromagnetic Engineering and Science*, vol. 18, no. 4, pp. 248-253, 2018. [CrossRef] [Google Scholar] [Publisher Link]

[10] Rajiv Kumar Singh, "EM Analysis of RF Interaction Structures for Gyrotron Devices," *Advances in VLSI, Communication and Signal Processing*, pp. 315-340, 2019. [CrossRef] [Google Scholar] [Publisher Link]